

High Velocity Compact Clouds in the Sagittarius C Region

Kunihiko Tanaka

ktanaka@phys.keio.ac.jp

Tomoharu Oka

Shinji Matsumura

*Department of Physics, Faculty of Science and Technology, Keio University, 3-14-1 Hiyoshi,
Yokohama, Kanagawa 223-8522 Japan*

Makoto Nagai

*Division of Physics, Faculty of Pure and Applied Sciences, University of Tsukuba, 1-1-1
Ten-noudai, Tsukuba, Ibaraki 305-8571 Japan*

and

Kazuhisa Kamegai

*Department of Industrial Administration, Faculty of Science and Technology, Tokyo University of
Science, 2641 Yamazaki, Noda, Chiba 278-8510 Japan*

ABSTRACT

We report the detection of extremely broad emission toward two molecular clumps in the Galactic central molecular zone. We have mapped the Sagittarius C complex ($-0^{\circ}.61 < l < -0^{\circ}.27$, $-0^{\circ}.29 < b < 0^{\circ}.04$) in the HCN $J = 4-3$, $^{13}\text{CO } J = 3-2$, and $\text{H}^{13}\text{CN } J = 1-0$ lines with the ASTE 10 m and NRO 45 m telescopes, detecting bright emission with $80-120 \text{ km s}^{-1}$ velocity width (in full-width at zero intensity) toward CO-0.30-0.07 and CO-0.40-0.22, which are high velocity compact clouds (HVCCs) identified with our previous CO $J = 3-2$ survey. Our data reveal an interesting internal structure of CO-0.30-0.07 comprising a pair of high velocity lobes. The spatial-velocity structure of CO-0.40-0.22 can be also understood as multiple velocity component, or a velocity gradient across the cloud. They are both located on the rims of two molecular shells of about 10 pc in radius. Kinetic energies of CO-0.30-0.07 and CO-0.40-0.22 are $(0.8-2) \times 10^{49}$ erg and $(1-4) \times 10^{49}$ erg, respectively. We propose several interpretations of their broad emission: collision between clouds associated with the shells, bipolar outflow, expansion driven by supernovae (SNe), and rotation around a dark massive object. These scenarios cannot be discriminated because of the insufficient angular resolution of our data, though the absence of visible energy sources associated with the HVCCs seems to favor the cloud-cloud collision scenario. Kinetic

energies of the two molecular shells are 1×10^{51} erg and 0.7×10^{51} erg, which can be furnished by multiple SN or hypernova explosions in 2×10^5 yr. These shells are candidates of molecular superbubbles created after past active star formation.

Subject headings: Galaxy: center

1. INTRODUCTION

It has long been recognized that the central molecular zone (CMZ) of our Galaxy is in a highly turbulent state. Large scale surveys in various molecular and atomic lines (Oka et al. 1998, 2012; Tsuboi et al. 1999; Martin et al. 2004; Riquelme et al. 2010b) show that the CMZ has anomalous physical and chemical conditions characterized by high density ($\sim 10^4$ cm $^{-3}$), high gas kinetic temperature (30–100 K), large velocity width ($\gtrsim 40$ km s $^{-1}$), and high abundance of SiO and complex organic molecules (Requena-Torres et al. 2006). The velocity dispersions of the molecular clouds in the CMZ are systematically larger by a factor of ~ 5 than those expected from the size–line width relation for the Galactic disk (Oka et al. 1998, 2001; Miyazaki & Tsuboi 2000; Shetty et al. 2012). There are also a number of spots with even broader emission than the usual CMZ clouds, whose velocity widths are ~ 100 km s $^{-1}$ (Martín-Pintado et al. 1997; Tsuboi et al. 1999; Oka et al. 1999). The CO $J = 3-2$ survey with the Atacama Submillimeter Telescope Experiment (ASTE) 10 m telescope (Oka et al. 2007; Nagai et al. 2007; Oka et al. 2012) detected a number of spots with high CO $J = 3-2/J = 1-0$ ratio (> 1.5), out of which about 70 were such clouds with very large velocity width. They have locally enhanced velocity dispersions and typically $\lesssim 3$ pc sizes, and in many cases are visible well in high density tracer lines as millimeter HCN, HCO $^+$, and submillimeter CO lines (Oka et al. 1999; Tanaka et al. 2007; Oka et al. 2012), indicating that they are shocked molecular features. They were named high velocity compact clouds (HVCCs) in Oka et al. (2007).

The velocity width of the largest HVCCs is ~ 100 km s $^{-1}$ in a full-width at zero intensity (FWZI; Oka et al. 1999, 2001, 2008). It is an open question what supports their fast internal motion, because the majority of the HVCCs lack apparent energy sources in their vicinity. Oka et al. (2008) hypothesized that one of the most energetic HVCC CO0.02–0.02 was created through interaction with a series of supernova (SN) explosions in a hidden massive stellar cluster. Tanaka et al. (2011) found the enhancement of the submillimeter atomic carbon line in this HVCC was similar to that seen in SN-shocked clouds in the Galactic disk (White 1994; Arikawa et al. 1999). Tanaka et al. (2007) investigated another energetic HVCC CO1.27+0.01 in the $l = 1^\circ.3$ complex and found that it was a part of a multiple expanding shell, which might evolve into a molecular superbubble. Their hypothesis suggests past micro-starburst activity in those regions. Alternatively, cloud–cloud collision at a high velocity can also create broad features. Such collisions may take place near the x_1 – x_2 orbit intersections (Hüttemeister et al. 1998; Riquelme et al. 2010a), or in the foot points of magnetic floated loops (Fukui et al. 2006; Torii et al. 2010; Riquelme et al. 2013).

In this paper we report the detection of strikingly broad and bright HCN $J = 4-3$ emission

toward two HVCCs, CO–0.40–0.22 and CO–0.30–0.07 (Oka et al. 2007, 2012), near the Sgr C giant molecular cloud (GMC) complex. They were first identified with the ASTE CO $J = 3-2$ survey (Oka et al. 2007, 2012), but their images suffered from severe contamination by surrounding less dense gas and absorption by the foreground Galactic disk, and hence their basic properties such as masses, sizes and velocity widths were unknown. We successfully obtained their uncontaminated images in full spatial and velocity extent in our HCN $J = 4-3$ data, owing to its very high critical density ($\sim 10^6 \text{ cm}^{-3}$). We also analyze kinematics of two newly found large molecular shells which are likely to be associated with the HVCCs. Based on these data we discuss several possible origins for the HVCCs, including past local starburst activity, interaction with compact supernova remnants (SNRs), and interaction with dark massive objects. We adopt 8.3 kpc for the distance to the Galactic center (Gillessen et al. 2009).

2. OBSERVATIONS

2.1. ASTE 10 m Observation

The HCN $J = 4-3$ (354.505 GHz) observations were performed with the ASTE 10 m telescope in 2010 August. We made an on-the-fly (OTF) mapping of a $20' \times 20'$ region centered at $(l, b) = (-0^\circ.45, -0^\circ.17)$, including a major part of the Sgr C complex and the gap region between the Sgr A and Sgr C regions. For convenience we refer to this region as the “Sgr C complex” in this paper, although it also contains clouds unassociated with the Sgr C H II region. We also made follow-up observations of the $^{13}\text{CO } J = 3-2$ line (330.588 GHz) in 2011 November and mapped $5' \times 5'$ regions centered at the HVCCs CO–0.30–0.07 and CO–0.40–0.22. The nomenclature of the HVCCs are basically taken from the molecular cloud catalog of Oka et al. (2012). CO–0.40–0.22 was cataloged as CO–0.41–0.23 in their list, but we use the former nomenclature in this paper because the latter does not represent the correct center position of the cloud.

In the ASTE observations a sideband-separation type receiver CATS345 was used as the receiver frontend. The telescope beam size at 350 GHz was $22''$. The reference position was taken at $(l, b) = (1^\circ, -1^\circ)$. As the backend, we used a 1024 ch auto-correlator system with a channel separation of 512 kHz corresponding to a 0.44 km s^{-1} velocity separation at 350 GHz. Typical system noise temperature during the observations was 200–300 K. Antenna pointing accuracy was maintained within $5''$ by CO $J = 3-2$ observations toward V1427 Aql. The antenna temperatures were calibrated with the standard chopper-wheel method. The total on-source integration time was 8 hr. The correction factor for the sideband rejection ratio and the main-beam efficiency was measured to be 1.8, by using M17SW as the intensity calibrator. The intensity reproducibility was within 10 % rms during the 11 observation days. After the subtraction of spectral baselines, the data were convolved with a Gaussian-tapered Bessel function and resampled onto a $8''.5 \times 8''.5 \times 2 \text{ km s}^{-1}$ grid by using the NOSTAR package developed at the Nobeyama Radio Observatory (NRO). The effective spatial resolution is $24''$. The rms noise level of the final maps is 0.13 K in T_{MB} for

the HCN $J = 4-3$ map, and 0.21 K for the $^{13}\text{CO } J = 3-2$ maps.

2.2. NRO 45 m Observation

We also made observations of $\text{H}^{13}\text{CN } J = 1-0$ (86.340 GHz) by using the BEARS 25 multi-beam receiver system on the NRO 45 m telescope in 2010 January. The same region covered by the ASTE observations was mapped with OTF scans. The telescope beam size at 86 GHz was $20''$. The digital backend was operated with the wide-band mode with a channel separation of 512 kHz corresponding to a 1.78 km s^{-1} velocity separation at 86 GHz. Antenna temperatures were calibrated by the standard chopper-wheel method. The correction factor for the main-beam efficiency ($1/\eta_{\text{MB}}$) was 2.5. Antenna pointing accuracy was maintained within $3''$ during the observation run by observing the $\text{SiO } J = 1-0$, $v = 1, 2$ maser lines toward VX Sgr. We created l - b - v_{LSR} data cube with a $8''.5 \times 8''.5 \times 2 \text{ km s}^{-1}$ grid and a $24''$ spatial resolution with the same procedure used for the ASTE data. The rms noise level of the final map is 0.08 K in T_{MB} .

3. RESULTS

Figure 1 shows velocity channel maps of HCN $J = 4-3$ and $\text{H}^{13}\text{CN } J = 1-0$ at 60 km s^{-1} velocity interval in the range from -130 km s^{-1} to $+110 \text{ km s}^{-1}$. This region contains multiple velocity components presumably at different line-of-sight positions (Liszt & Spiker 1995; Lang et al. 2010; Riquelme et al. 2010b). The first and second channels in Figure 1 roughly correspond to the -100 km s^{-1} and -65 km s^{-1} clouds in the nomenclature in Lang et al. (2010), or to the clouds 10 and 11 in the nomenclature in Riquelme et al. (2010b). The Sgr C H II region is associated with the latter component (Liszt & Spiker 1995). The cloud in the southern part ($l, b = -0^\circ.4, -0^\circ.2$) of the third velocity channel is not a Galactic center source but is associated with the H II region RCW137 at a distance of 1.5 kpc (Russeil 2003).

We detected remarkably intense emission toward compact clouds CO-0.40-0.22 and CO-0.30-0.07, whose peak HCN $J = 4-3$ integrated intensities are 530 K km s^{-1} and 250 K km s^{-1} , respectively, whereas the intensity does not exceed 120 K km s^{-1} even in the densest part of the GMC main component. They are both identified as HVCCs in Oka et al. (2012) on the basis of their CO $J = 3-2$ survey data, but they are less bright in the CO line and heavily contaminated with less dense, spatially extended gas. In our HCN $J = 4-3$ map they are well isolated from the main component of the GMC complex and their extraordinarily large velocity width is clearly seen. Figure 2 shows Galactic longitude-velocity diagrams of HCN $J = 4-3$ at $1'$ latitude interval. In the figure CO-0.40-0.22 ($b = -14'$ to $-13'$) and CO-0.30-0.07 ($b = -4'$ to $-3'$) are seen as bright broad line features with 80 km s^{-1} and 120 km s^{-1} FWZI, respectively, whereas the velocity width is $\sim 20 \text{ km s}^{-1}$ for other regions in the map.

Their velocity widths are notably large even compared with other HVCCs identified in Oka et al.

(2012). Most of the HVCCs detected with CO observations have $\sim 50 \text{ km s}^{-1}$ FWZI or smaller velocity width, with only a few exceptions such as CO0.02–0.02 and CO1.27+0.01 (Tanaka et al. 2007; Oka et al. 2008). We list the parameters of CO–0.40–0.22 and CO–0.30–0.07 in Table 1.

We also find that the HVCCs are located close to two large molecular shells, whose positions are shown in Figure 1. The shell 1 has a well-defined ellipse morphology with a position angle of 50° in the Galactic coordinate. The HVCC CO–0.30–0.07 is located on the eastern edge of this shell. The shell 2 is in the southernmost part of the Sgr C region in the velocity range from -130 to -10 km s^{-1} . The upper and lower parts of the shell 2 appear in different velocity ranges in Figure 1, and its elliptical shape is more clearly visible in the integrated intensity map shown in Figure 3. The HVCC CO–0.40–0.22 is located on the rim of the shell 2. In Table 1 we listed the center positions, diameters, and position angles of the shells determined with eye-fitting.

3.1. Spatial-Velocity Structure of the HVCCs

Our HCN $J = 4-3$ data reveals an interesting internal spatial-velocity structure of the HVCCs. Figure 4 presents position–velocity ($P - V$) diagrams of CO–0.30–0.07 and CO–0.40–0.22 in HCN $J = 4-3$, $\text{H}^{13}\text{CN } J = 1-0$, and $^{13}\text{CO } J = 3-2$ made along the A–A' and B–B' cuts shown in Figure 3. We see that CO–0.30–0.07 is not a single-profiled clump but a composition of blue- and red-shifted high velocity lobes. Each lobe has 50 km s^{-1} velocity width in FWZI, and they are sharply separated from each other both spatially and in velocity. We cannot clearly see the internal structures of the other HVCC, CO–0.40–0.22, but its peak positions at the low and high velocity ends differ by $20''$. This can be understood as unresolved multiple velocity components or as a velocity gradient across the cloud.

It is not likely that the double-lobed CO–0.30–0.07 is a chance superposition of two unrelated clouds. Firstly, high density gas is scarce in the v_{LSR} range higher than 50 km s^{-1} as shown in the Figures 1 and 2, and therefore it would be unreasonable to assume that a peculiar broad feature in this velocity range falls along the same line-of-sight as another peculiar cloud by chance. In addition, their morphology implies that they are physically related to each other. Figure 5 shows HCN $J = 4-3$ integrated intensity maps of the red- and blue-shifted lobes, in which they show a clear spatial anti-correlation. In particular, the arched shape of the red-shifted lobe is in a good accordance with the curvature of the right edge of the blue-shifted lobe. Therefore, it is more plausible that they are interacting clouds, or represent different portions of a systematic motion such as expansion or rotation.

The compact broad line features are also visible in $\text{H}^{13}\text{CN } J = 1-0$ and $^{13}\text{CO } J = 3-2$ but less clearly, for the both HVCCs. The ^{13}CO line has a relatively low critical density of 10^4 cm^{-3} , and hence is more sensitive to less dense, quiescent molecular gas invisible in HCN $J = 4-3$, such as the narrow line component at $v_{\text{LSR}} \sim 10 \text{ km s}^{-1}$ near CO–0.30–0.07 (Figure 4). In particular the $^{13}\text{CO } J = 3-2$ map of CO–0.40–0.22 is dominated by spatially extended broad emission of

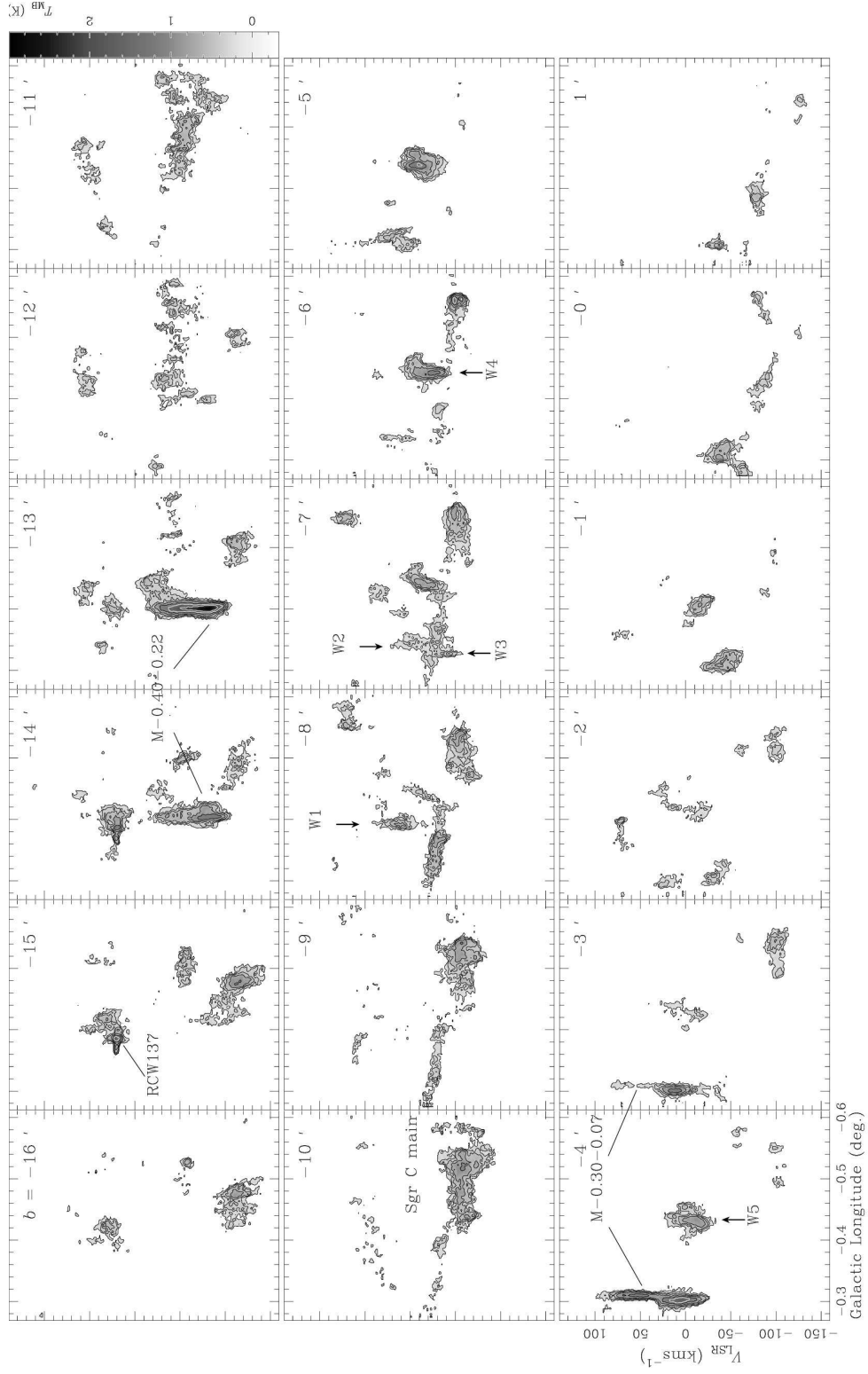


Fig. 2.— Longitude-velocity diagrams of HCN $J = 4-3$. Contour levels are 3, 5, 7, 10, 15, 20, and 30 K. The labels W1–5 denote the positions of the moderately broad line features associated with the shell 1 (Section 3.3).

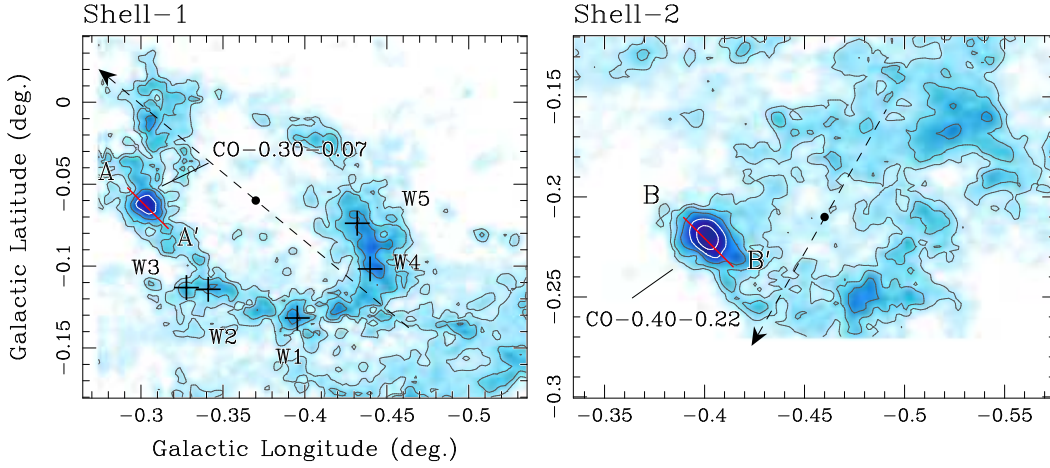


Fig. 3.— HCN $J = 4-3$ integrated intensity maps near (a) the shell 1 and (b) the shell 2. Integration velocity range is from -60 km s^{-1} to 50 km s^{-1} for shell 1 and from -150 km s^{-1} to -20 km s^{-1} for shell 2. Contour levels are 5, 10, 20, 40, 80, and 160 K km s^{-1} . The labels W1–5 denote the positions of the moderately broad line features (Section 3.3). The broken lines are the major axis of the shells determined by eye-fitting. The center positions are denoted by dots. The lines A–A' and B–B' are the strip lines along which the position–velocity diagrams of the HVCCs (Figure 4) are made.

Table 1. Parameters of HVCCs and Shells

	CO–0.30–0.07	CO–0.40–0.22	Shell-1	Shell-2
Center (l, b)	$(-0^\circ.30, -0^\circ.07)$	$(-0^\circ.40, -0^\circ.22)$	$(-0^\circ.37, -0^\circ.06)$	$(-0^\circ.46, -0^\circ.21)$
Diameter (pc)	3.6	4.3	24×16	16×12
Position Angle	—	—	50°	-30°
Velocity Dispersion (km s^{-1}) ^a	20	18	—	—
Expansion Velocity (km s^{-1}) ^b	—	—	(40)	35
Mass (M_\odot) ^c	2×10^3	4×10^3	9×10^4	6×10^4
Kinetic Energy (erg) ^d	$(0.8-2) \times 10^{49}$	$(1-4) \times 10^{49}$	1×10^{51}	0.7×10^{51}

^aFrom $\text{H}^{13}\text{CN } J = 1-0$ data.

^bSee Section 3.3.

^cFrom $\text{H}^{13}\text{CN } J = 1-0$ and HCN $J = 4-3$ luminosity. See Section 3.5.

^dSee Section 3.5.

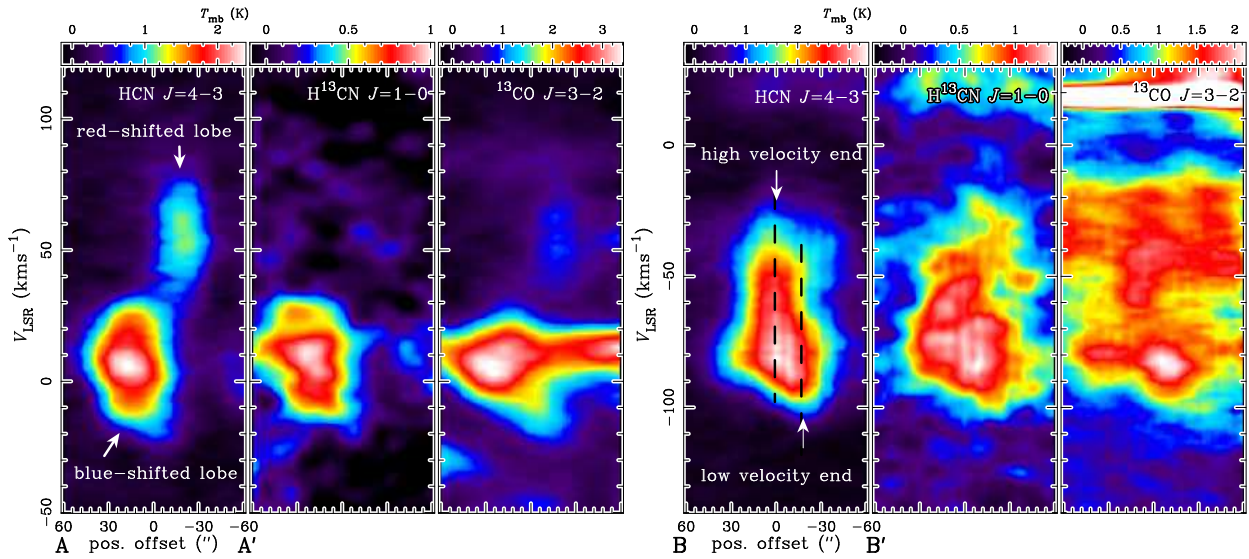


Fig. 4.— Position-velocity (P - V) diagrams of the HVCCs in HCN $J = 4-3$, $\text{H}^{13}\text{CN } J = 1-0$, and $^{13}\text{CO } J = 3-2$, for CO-0.30-0.07 (left; along the A-A' cut in Figure 3) and for CO-0.40-0.22 (right; along the B-B' cut in Figure 3). The broad line features composing the HVCCs are the most clearly visible in the HCN $J = 4-3$ maps, whereas the $^{13}\text{CO } J = 3-2$ maps are more sensitive to less dense, spatially extended components such as the narrow line feature at $v_{\text{LSR}} = 10 \text{ km s}^{-1}$ in the CO-0.30-0.07 map, and the broad features extended throughout the CO-0.40-0.22 map.

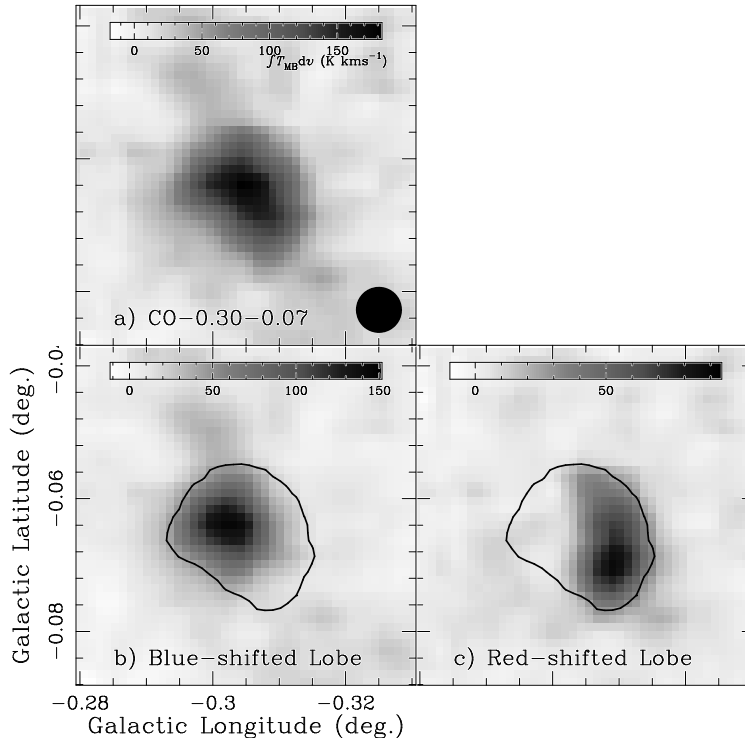


Fig. 5.— HCN $J = 4-3$ integrated intensity maps of CO-0.30-0.07, made for the full velocity range (a ; -30 km s^{-1} to $+100 \text{ km s}^{-1}$), for the blue-shifted lobe (b; -30 km s^{-1} to $+30 \text{ km s}^{-1}$) and for the red-shifted lobe (c; $+40 \text{ km s}^{-1}$ to $+100 \text{ km s}^{-1}$). Contours of integrated intensity of 50 K km s^{-1} over the full velocity range are drawn in the panels b and c. The filled circle on the panel a denotes the effective beam size ($24''$).

the shell 2, whose velocity extent is equal to that of the HVCC. The H^{13}CN map has intermediate characteristics between those of HCN $J = 4-3$ and ^{13}CO : isolated broad feature is present but is spatially more extended than in HCN.

3.2. Images of the HVCCs in Other Wavelengths

Currently no bright continuum sources are known toward CO-0.40-0.22 and CO-0.30-0.07. Figure 6 shows radio and far-infrared continuum ($\lambda = 20 \text{ cm}, 75 \mu\text{m}$, and $500 \mu\text{m}$) maps near CO-0.30-0.07 and CO-0.40-0.22 taken from the data archives of the Very Large Array (VLA) and the *Herschel Space Observatory*. The $500 \mu\text{m}$ emission traces the column density of the cold dust ($T \sim 20 \text{ K}$; Pierce-Price et al. 2000). We see small $500 \mu\text{m}$ emission excess both toward CO-0.30-0.07 and toward CO-0.40-0.22. This dimness in $500 \mu\text{m}$ indicates that the very bright HCN emission of the HVCCs is because of high excitation temperatures rather than because of

high column density of the clouds. The 20 cm and 75 μm maps show neither of CO–0.30–0.07 nor CO–0.40–0.22 are associated with bright thermal or non-thermal compact sources indicative of young massive stars or SNRs. The bright sources in 20 cm and 75 μm to the southeast of CO–0.40–0.22 is from the foreground H II region RCW137. Two 20 cm sources are also seen in the vicinity of CO–0.40–0.22, a non-thermal radio filament C1 and a point source G359.58–0.24 with unknown nature (Yusef-Zadeh et al. 2004), but no evidence to imply their association to the cloud is found.

3.3. Expansion Motion of the Shells

Figure 7 shows $P - V$ diagrams of the shells 1 and 2 in HCN $J = 4-3$, cut along their major axes (shown in Figure 3) and averaged over the minor axis extent. Both shells have very large velocity extent of about 100 km s^{-1} . In addition to the HVCCs CO–0.30–0.07 and CO–0.40–0.22 at the left edges, a very broad feature is present at the right edge of the shell 1, whose width is comparable to that of the HVCCs. This large velocity feature shows curvature in the $P - V$ space, which could be understood as a part of an elliptical pattern expected for a shell with a radial expansion motion. The expansion velocity is roughly estimated to be 40 km s^{-1} . However, the left edge of the shell, i.e., CO–0.30–0.07 does not have a curvature consistent with this expanding shell model, and it is unclear whether the entire shell has an expansion motion. On the other hand, the entire part of the shell 2 can be relatively well fitted by a partial elliptical pattern, except for the velocity higher than -40 km s^{-1} , where the higher velocity part of CO–0.40–0.22 does not follow the curvature of the partial ellipse. The expansion velocity of the shell 2 is estimated to be 35 km s^{-1} .

In addition to the above broad velocity features, moderately broad features of about $40-50 \text{ km s}^{-1}$ velocity width are associated with the shell 1 (Figure 2). These moderately broad emission features are denoted by labels W1–5 in Figures 2 and 3. The features W3, 4, and 5 form the broad emission at the right edge of the shell 1 in Figure 7. We note that the moderately broad emission features appear exclusively on the rim of the shell 1.

3.4. Physical Conditions of HVCCs

The noteworthy HCN $J = 4-3$ brightness of the HVCCs indicates their unusual physical conditions. We calculate the T_{kin} and n_{H} ranges to reproduce the observed HCN $J = 4-3/\text{H}^{13}\text{CN } J = 1-0$ ratios of CO–0.30–0.07 and CO–0.40–0.22, which are 2.6 and 2.5, respectively, by employing the large velocity gradient (LVG) model (Goldreich & Kwan 1974). We assume that the $[\text{HCN}]/[\text{H}^{13}\text{CN}]$ isotopic abundance ratio is 24 (Langer & Penzias 1990, 1993) and calculate the intensity ratio for the dN_{HCN}/dv range of $10^{13-15} \text{ cm}^{-2} (\text{km s}^{-1})^{-1}$. The rate coefficients are taken from the Leiden atomic and molecular database (Schöier et al. 2005). The calibration error of 10 % in the line intensities are considered in the calculations. We also perform the same calculation

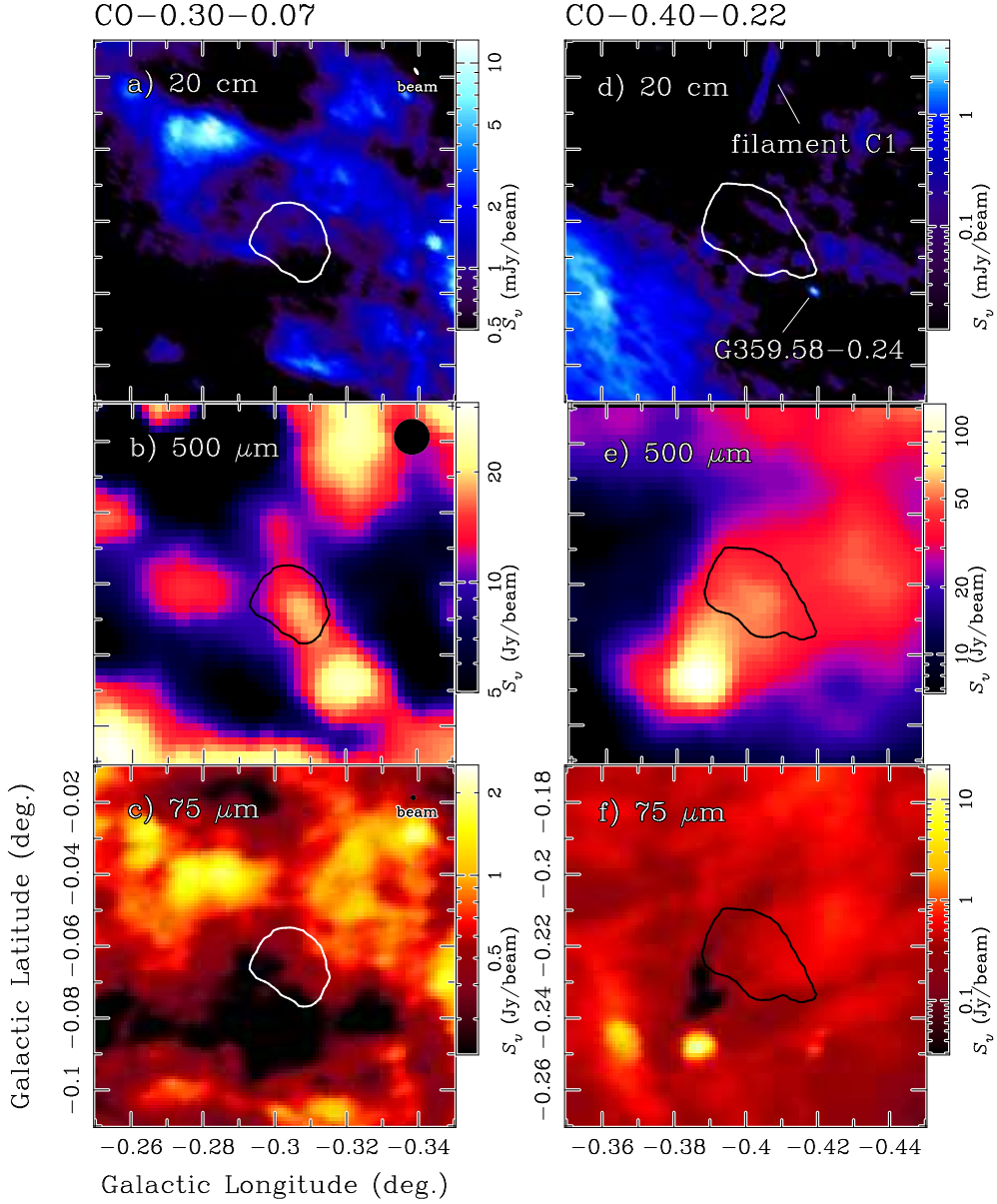


Fig. 6.— Continuum maps of 20 cm, 500 μm , and 75 μm wavelengths near CO-0.30-0.07 (left) and CO-0.40-0.22 (right). The 20 cm maps are taken from the VLA archival data, and the 500 and 75 μm maps are from the *Herschel* archival data. The contours are drawn at an HCN $J = 4-3$ integrated intensity level of 50 Kkm s^{-1} . Spatial resolution is denoted by a filled circle for each map. We see counterparts of the HVCCs in the 500 μm images, but not for the 75 μm and the 20 cm images.

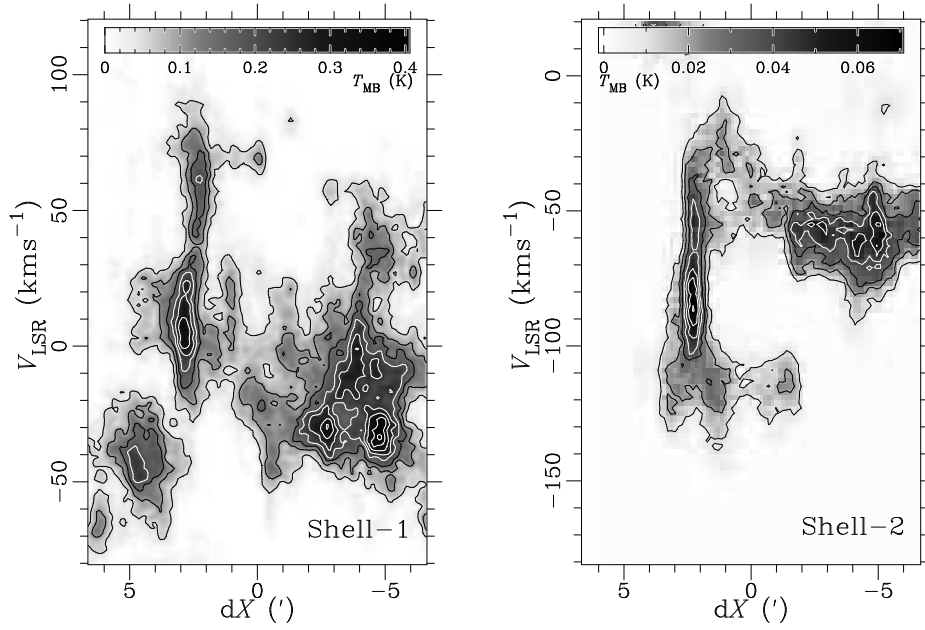


Fig. 7.— Position–velocity diagrams of the shell 1 (left) and the shell 2 (right) made along their major axes. Emission is averaged over the full extent in the direction of the minor axes. The relative distance dX is measured from the center position of the shell in the direction denoted by the arrows in Figure 3. Contours are drawn at every 0.05 K for the shell 1, and at every 0.01 K for the shell 2.

for the ‘quiescent component’ for purpose of comparison, which we define as the pixels that do not belong to either of the HVCCs, the two molecular shells, or the foreground RCW137 region. Calculations are performed separately for the -65 km s^{-1} and -100 km s^{-1} clouds of the quiescent component, whose representative HCN $J = 4-3/\text{H}^{13}\text{CN } J = 1-0$ ratios are 0.8 and 0.6, respectively.

The results are shown in Figure 8. The physical conditions of the quiescent component are consistent with those of the typical CMZ clouds from preceding studies (e.g. Martin et al. 2004; Nagai et al. 2007) in that $n_{\text{H}} = 10^{3.5-4} \text{ cm}^{-3}$ and $T_{\text{kin}} = 30-100 \text{ K}$. The HVCCs have much higher density and possibly higher temperature than them. When compared at a T_{kin} of 50 K, the density of the -65 km s^{-1} cloud is less than 10^5 cm^{-3} , whereas the density of HVCCs is $10^{5.5-6.5} \text{ cm}^{-3}$. Our analysis sets upper limits for the kinetic temperatures of the quiescent component, which are 160 K and 110 K for the -65 and -100 km s^{-1} cloud. On the other hand, much higher temperature of $> 200 \text{ K}$ is allowed for the HVCCs. This highly enhanced density and possibly temperature, along with the large velocity width, confirms that the HVCCs are shocked features.

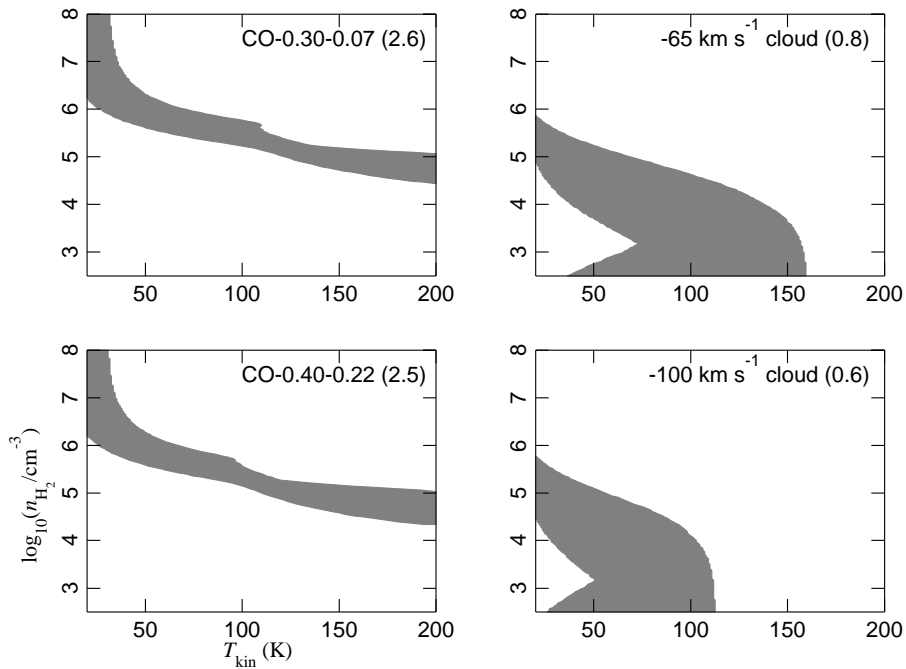


Fig. 8.— Ranges of T_{kin} and n_{H} calculated with LVG analysis of the HCN $J = 4-3/\text{H}^{13}\text{CN } J = 1-0$ intensity ratios for the HVCCs (CO–0.30–0.07 and CO–0.40–0.22) and the quiescent clouds (-65 km s^{-1} cloud and -100 km s^{-1} cloud). The shaded areas are the parameter ranges which reproduce the observed HCN $J = 4-3/\text{H}^{13}\text{CN } J = 1-0$ ratios (written in the parenthesis) within 10 % accuracy. A dN_{HCN}/dv range of $10^{13-15} \text{ cm}^{-2} (\text{km s}^{-1})^{-1}$ is assumed in the calculations.

3.5. Mass and Kinetic Energy of the HVCCs and the Shells

We estimate masses of the HVCCs from their HCN $J = 4-3$ and $\text{H}^{13}\text{CN } J = 1-0$ luminosity. If the $\text{H}^{13}\text{CN } J = 1-0$ transition is not optically thick, we can obtain a good estimate of the HCN column density from the LVG analysis in the previous section. By assuming the $[\text{HCN}]/[\text{CO}]$ and $[\text{H}^{13}\text{CN}]/[\text{H}_2]$ abundance ratios to be $10^{-2.7}$ and 10^{-6} , respectively (Lis & Goldsmith 1989, 1990; Tanaka et al. 2009), the conversion factor from the $\text{H}^{13}\text{CN } J = 1-0$ flux to mass is calculated to be $87 \pm 3 M_\odot (\text{K km s}^{-1} \text{ arcmin}^2)^{-1}$ from their HCN $J = 4-3/\text{H}^{13}\text{CN } J = 1-0$ ratios, on the condition that $30 \text{ K} < T_{\text{kin}} < 200 \text{ K}$, $10^{2.5} \text{ cm}^{-3} < n_{\text{H}} < 10^8 \text{ cm}^{-3}$, and the $\text{H}^{13}\text{CN } J = 1-0$ optical depth is less than 0.5. The $\text{H}^{13}\text{CN } J = 1-0$ flux is $20 \text{ K km s}^{-1} \text{ arcmin}^2$ for CO–0.30–0.07 and $40 \text{ K km s}^{-1} \text{ arcmin}^2$ for CO–0.40–0.22, which are converted into masses of $2 \times 10^3 M_\odot$ and $4 \times 10^3 M_\odot$, respectively. These masses are similar to those of normal CMZ clouds identified with the CS $J = 1-0$ survey of Tsuboi et al. (1999). The masses of the CS clouds of 3–4 pc in diameter (i.e., similar sizes to CO–0.40–0.22 and CO–0.30–0.07) are in a range from $5 \times 10^3 M_\odot$ to $4 \times 10^4 M_\odot$ (Miyazaki & Tsuboi 2000). The CS luminosity mass of CO–0.40–0.22, or the cloud 32 in their nomenclature, is $5.9 \times 10^3 M_\odot$, being consistent with our estimate.

We also check the above mass estimates by comparing them with masses estimated from 500 μm luminosity. It is known that the cold dust temperature is not coupled with the gas temperature in the CMZ, and is relatively low and uniform throughout the region (Pierce-Price et al. 2000, and references therein). By assuming a dust temperature of 20 K and the dust emissivity index (β) of 2, the mass (M) is derived as $M/M_\odot = 83 S_{500}/\text{Jy}$ from 500 μm flux density (S_{500}), including the correction factor of 2 for the high metallicity in the CMZ (Pierce-Price et al. 2000, and references therein). The 500 μm flux density of CO–0.30–0.07 is measured to be 12 Jy, which gives a mass of $1 \times 10^3 M_\odot$. This is a good agreement with the HCN luminosity mass of $2 \times 10^3 M_\odot$, considering large uncertainties in the dust-to-gas ratio, the $[\text{H}^{13}\text{CN}]/[\text{H}_2]$ abundance ratio, and the dust temperature.

We estimate the kinetic energies of the HVCCs on the basis of the above mass estimates with the equation $E_{\text{kin}} = \frac{1}{2}\alpha M\sigma_v^2$, where σ_v is mass-weighted velocity dispersion. The factor α (> 1) is a correction for the projection effect. The values of σ_v of CO–0.30–0.07 and CO–0.40–0.22 are 20 km s^{-1} and 18 km s^{-1} in $\text{H}^{13}\text{CN } J = 1-0$, respectively, which yields the kinetic energies of $\alpha \cdot 0.8 \times 10^{49} \text{ erg}$ and $\alpha \cdot 1.2 \times 10^{49} \text{ erg}$. The factor α is 3 for the case of isotropic velocity dispersion, and 1 for the case that the velocity dispersion exists only in the line-of-sight direction. Hence we estimate the range of the kinetic energy to be $(0.8-2) \times 10^{49} \text{ erg}$ for CO–0.30–0.07, and $(1-4) \times 10^{49} \text{ erg}$ for CO–0.40–0.22.

We also estimate the mass of the shells 1 and 2 with the same procedure used for the HVCCs. The H^{13}CN flux to mass conversion factor for the shells is calculated to be $88 \pm 2 M_\odot (\text{K km s}^{-1} \text{ arcmin}^2)^{-1}$ from the HCN $J = 4-3/\text{H}^{13}\text{CN } J = 1-0$ ratio of 0.8. The H^{13}CN flux associated with the shell is $1 \times 10^3 \text{ K km s}^{-1} \text{ arcmin}^2$ for the shell 1 and $7 \times 10^2 \text{ K km s}^{-1} \text{ arcmin}^2$ for the shell 2, which are converted into masses of $9 \times 10^4 M_\odot$ and $6 \times 10^4 M_\odot$, respectively. Their kinetic energy of

the expansion motion of the shells is given by $\frac{1}{2}M v_{\text{exp}}^2$, which is 1×10^{51} erg for the shell 1 and 0.7×10^{51} erg for the shell 2 when the v_{exp} values of 40 km s^{-1} and 35 km s^{-1} are adopted for the shells 1 and 2, respectively. We list the masses and kinetic energies of the shells in Table 1, along with the results for CO–0.40–0.22 and CO–0.30–0.07.

4. DISCUSSION

4.1. Possible Origins of CO–0.40–0.22 and CO–0.30–0.07

We have shown that the HVCCs in the Sgr C complex, CO–0.40–0.22 and CO–0.30–0.07, have bright HCN $J = 4-3$ emission and large velocity width of $80-100 \text{ km s}^{-1}$, in spite of their small diameters of about 4 pc. They lie a factor of 20 above the size–line width relation for the Galactic disk, and about a factor of 4 above that for the CMZ (Shetty et al. 2012, and references therein). Their velocity widths are notably large even compared with the other HVCCs found with previous CO surveys. Our HCN $J = 4-3$ observations have also revealed their internal spatial-velocity structure: the double high velocity lobes of CO–0.30–0.07 and velocity gradient of CO–0.40–0.22. We examine the origin of CO–0.40–0.22 and CO–0.30–0.07, in terms of cloud–cloud collision, bipolar outflow, expansion motion, and rotation.

4.1.1. Cloud–Cloud Collision

The double-lobed structure of CO–0.30–0.07 is readily explained if we assume that it is a pair of colliding clouds. The velocity gradient of CO–0.40–0.22 could be also understood as unresolved multiple velocity components. An advantage of this cloud–cloud collision interpretation is that it does not require energy sources at the positions of the HVCCs, and hence can explain the absence of bright continuum emission associated with them.

The HVCCs are both located on the rim of large molecular shells which have signs of expansion motion. The $^{13}\text{CO } J = 3-2$ map of CO–0.40–0.22 (Figure 4) especially gives the impression that the broad HCN of the HVCCs is a part of a spatially extended ^{13}CO emission of the shell 2. We also note that the simple expansion models for the shells deviate from the observations at the positions of the HVCCs. These situations may imply that the HVCCs are points where the expanding shells are colliding with dense gas in the outside quiescent component. The maximum turbulent velocity which can be caused by collision is roughly equal to the velocity difference between the colliding clouds, which is expected to be similar to the expansion velocity v_{exp} of the shell. The v_{exp} values of the shells (40 km s^{-1} and 35 km s^{-1} for the shells 1 and 2, respectively) are consistent with the velocity dispersion of the HVCCs, which is 20 km s^{-1} for CO–0.30–0.07 and 18 km s^{-1} for CO–0.40–0.22. The moderately broad line features associated with the shell 1 can be also considered as similar collision points associated with the shell. This scenario is related to another

problem of energy sources of the shells 1 and 2, about which we discuss in the Section 4.2.

We could consider other processes that cause cloud–cloud collisions associated with large-scale dynamics in the CMZ. Broad molecular emission is reported at the foot-points of the magnetic floated loops in outer region of the CMZ (Fukui et al. 2006; Torii et al. 2010). However, evidently neither of the HVCCs in the Sgr C complex are associated with loop-like molecular structures. Riquelme et al. (2010a) identified a high velocity cloud at $l \sim 1^\circ.3$ to be a cloud falling from the x_1 orbit, on the basis of its high $^{12}\text{C}/^{13}\text{C}$ isotopic ratio characteristic for the x_1 orbit clouds. We evaluated the $^{12}\text{C}/^{13}\text{C}$ isotopic ratio of CO–0.40–0.22, but did not obtain positive results for low ^{13}C abundance. The $\text{HCO}^+ J=1-0/\text{H}^{13}\text{CO}^+ J=1-0$ and the $\text{HNC } J=1-0/\text{HN}^{13}\text{C } J=1-0$ intensity ratios of CO–0.40–0.22 measured from the data by Jones et al. (2012) are 18 ± 3 and 14 ± 3 , respectively, for the -100 km s^{-1} to -60 km s^{-1} velocity range of CO–0.40–0.22. These ratios are lower than the $^{12}\text{C}/^{13}\text{C}$ ratio (40–70) measured for the x_1 orbit cloud (Riquelme et al. 2010a) and is consistent with the typical value for the x_2 orbit clouds (24; Langer & Penzias 1990, 1993). For CO–0.30–0.07 we could not evaluate the isotopic ratios because of an insufficient signal-to-noise ratio.

4.1.2. Bipolar Outflow

The appearance of the HVCCs is similar to that of extremely high velocity (EHV) CO emission of molecular outflow sources (Bachiller & Cernicharo 1990; Leurini et al. 2006; Qiu et al. 2011). There are spots of intense 44.07 GHz methanol emission toward the both HVCCs (Jones et al. 2013), and they are possibly class-I maser sources which are commonly detected toward molecular outflow sources. In addition, intense SiO lines, which are well-established tracers of molecular outflows, are also detected toward CO–0.40–0.22 (Jones et al. 2011, 2013).

However, the kinetic energy of the known EHV sources is at most 9×10^{47} erg (Leurini et al. 2006), which is about an order of magnitude smaller than that of the HVCCs. Any YSO candidates are so far not detected in IR images (Yusef-Zadeh et al. 2009; Immer et al. 2012) nor in OH or class-I methanol maser data (Yusef-Zadeh et al. 1999; Caswell et al. 2010). Therefore, it is unlikely that the HVCCs are bipolar outflow sources, unless we assume a peculiar driving source which is deeply embedded and extremely energetic.

4.1.3. Compact Expanding Shell

The double-lobe of the CO–0.30–0.07 can be also interpreted as an unresolved, compact expanding shell. In this interpretation, the red- and blue-shifted lobes are assumed to represent the hemispheres with the receding and approaching line-of-sight velocity. The kinetic energy of the HVCCs of 10^{49} erg order is consistent with the energy injected to molecular clouds by a single SN explosion (e.g. Moriguchi et al. 2001; Sashida et al. 2013). High velocity molecular emission with

80–120 km s⁻¹ velocity width is also detected toward IC443 and W44 SNRs (Dickman et al. 1992; Sashida et al. 2013).

An argument against this SNR hypothesis is that the HVCCs lack radio and X-ray emission indicative of SNRs. The dynamical age of the assumed compact shell is $D/\Delta v = 10^4$ yr, where D and Δv are diameter and FWZI velocity width of the HVCC. It is an open question whether it is possible that a SNR with this relatively young age does not show detectable emission. The lack of radio continuum emission may be partly explained by deficiency of relativistic electrons owing to the strong magnetic field (Oka et al. 2001) and by intense background non-thermal radio emission widespread in the CMZ (LaRosa et al. 2005).

4.1.4. Rotating Ring/Disk

We also consider the possibility that the large velocity width of the HVCCs comes from rotation motion. The double-lobed structure of CO–0.30–0.07 and the velocity gradient of CO–0.40–0.22 could be interpreted as the rotation of a ring or disk viewed from edge-on. The mass enclosed inside a rotating ring with a radius r and a rotation velocity v_{rot} is rv_{rot}^2/G , where G is the gravitational constant. When we assume the velocity width of the HVCCs is due to the rotation plus the intrinsic velocity width of 20 km s⁻¹, and that the radii are the half distance between the highest and lowest velocity peaks (0.6 pc and 0.4 pc for CO–0.30–0.07 and CO–0.40–0.22, respectively), the enclosed mass is estimated to be $1 \times 10^5 M_{\odot}$ for CO–0.40–0.22 and $3 \times 10^4 M_{\odot}$ for CO–0.30–0.07. A candidate of a compact massive object with this huge mass is an intermediate-mass black hole (IMBH), which might have been formed through runaway stellar mergers in a compact cluster, or brought from a satellite galaxy by a minor-merger event (Ebisuzaki et al. 2001; Portegies Zwart et al. 2004). Candidates of IMBHs are found as ultra luminous X-ray sources in external galaxies (Colbert & Mushotzky 1999), but no bright X-ray sources are known near the HVCCs.

The above possible explanations for the large velocity width of CO–0.40–0.22 and CO–0.30–0.07, namely, collision, bipolar outflow, expansion, and rotation cannot be strictly discriminated with our data because of the insufficient spatial resolution of our data taken with single-dish telescopes. At present, the absence of visible energy sources at any wavelength seems to favor the collision scenario, because other scenarios require energy sources inside or in the vicinity of the HVCCs. In particular, in the bipolar outflow and rotating ring/disk scenarios we assume very exotic objects such as extremely energetic outflow-driving stars and IMBHs as the energy sources. A more detailed investigation based on interferometric observations would be required to conclude whether the spatial-velocity structure of the HVCCs demands the presence of such objects.

4.2. Energy Sources of Molecular Shells: Multiple Supernovae/Hypernovae?

The well-defined elliptical structure of the shells and their signs of expansion motion suggest that each of them was created by a point explosion. A typical core-collapse SN event supplies baryonic energy of 10^{51} erg to interstellar space. Considering that 0.01–0.1 of the total SN energy is passed into molecular clouds (e.g. Dickman et al. 1992; Sashida et al. 2013), about more than 10 SN explosions or two hypernova (HN) explosions could explain the total kinetic energy of the shells. Dynamical age is $R/v_{\text{exp}} = 2 \times 10^5$ yr for both shells, and hence this hypothesis requires an SN/HN rate of 10^{-5} to 10^{-4} yr $^{-1}$. This SN/HN rate is not an unrealistic value compared with the SN rate of the Galaxy ($1.9 \pm 1.1 \times 10^{-2}$ yr $^{-1}$; Diehl et al. 2006), because if we roughly scale the molecular mass to the SN rate, the SN rate of the Sgr C complex is $(2-8) \times 10^{-5}$ yr $^{-1}$ from the 500 μm luminosity mass of the region ($2.5 \times 10^6 M_{\odot}$) and the total Galactic H $_2$ mass ($\sim 10^9 M_{\odot}$; Bloemen et al. 1986).

The SN rate gives an estimate of the star formation rate (SFR) of $\sim 10^7$ yr ago. If we assume that 10 SN explosions took place in their dynamical age, and that stars heavier than $8 M_{\odot}$ cause SN explosions, the past SFR of the Sgr C region is estimated to be $5 \times 10^{-3} M_{\odot} \text{yr}^{-1}$ on assumption of a Kroupa initial mass function (IMF; Kroupa 2001) with an upper mass cut-off of $50 M_{\odot}$. Alternatively, if we assume that two HN explosions took place in 2×10^5 yr, i.e., one HN for each shell in their dynamical time, and that stars heavier than $40 M_{\odot}$ cause HN explosions, the SFR is $3 \times 10^{-2} M_{\odot} \text{yr}^{-1}$. With these assumptions and by using the 500 μm luminosity mass, the star formation efficiency (SFE) of 10^7 yr ago is estimated to be $(0.2-1) \times 10^{-8}$ yr $^{-1}$. This does not reconcile with the present-day SFE of the CMZ ($1-3.4 \times 10^{-10}$ yr $^{-1}$; Yusef-Zadeh et al. 2009), but is more consistent with the high SFR values at 10^{5-6} yr ago suggested by infrared observations ($0.07-0.14 M_{\odot} \text{yr}^{-1}$ for the entire CMZ; Yusef-Zadeh et al. 2009; Immer et al. 2012) which yields a SFE value of $\sim 1 \times 10^{-9}$ yr $^{-1}$.

Hence, the large molecular shells 1 and 2 are candidates of molecular superbubbles created after past active star formation, similar to those found in the $l = 1^{\circ}.3$ and Sgr B1 complexes (Tanaka et al. 2007, 2009). The Sgr C complex is in fact rich in young stars of ages 10^{5-6} yr. Yusef-Zadeh et al. (2009) identified 21 YSOs of 10^5 yr age in a mass range from $5.4 M_{\odot}$ to $9.5 M_{\odot}$ in the 24 μm map of this region, from which the SFR of the Sgr C region at 10^5 yr ago is estimated to be $2 \times 10^{-2} M_{\odot} \text{yr}^{-1}$ with the Kroupa IMF. The above SFR value required for the formation of the shells 1 and 2 is not unreasonably high compared with this value. As shown in our observations, the present Sgr C complex is not rich in high density molecular gas compared to the Sgr A and Sgr B complexes, and is accordingly inactive in star formation except for the vicinity of the Sgr C H II region. The coincidence of the ages of the shells and the YSOs may mean that the superbubbles cleared up the molecular gas in this region, terminating the active star formation phase which had lasted until $\sim 10^5$ yr ago.

5. SUMMARY

We present HCN $J = 4-3$ and $\text{H}^{13}\text{CN } J = 1-0$ images of the Sgr C GMC complex taken with the ASTE 10 m and NRO 45 m telescopes. Below we summarize the main results.

1. We detected strikingly intense HCN $J = 4-3$ emission toward the two compact clouds, CO–0.30–0.07 and CO–0.40–0.22, whose integrated intensities are more than a factor of 2 brighter than that in any other part in the complex. They are HVCCs with very large velocity widths of $\sim 100 \text{ km s}^{-1}$ FWZI. CO–0.30–0.07 has a distinctive double-lobed structure with a 120 km s^{-1} velocity width. CO–0.40–0.22 has an 80 km s^{-1} velocity width, whose spatial-velocity structure can be also understood as multiple velocity component or velocity gradient.
2. We also found two shells of about 10 pc radius each. They both consist of very broad molecular emission with signs of expansion motion. If they have expansion motion, the radial expansion velocity is estimated to be 40 km s^{-1} and 35 km s^{-1} for the shells 1 and 2, respectively.
3. We made an LVG analysis with the HCN $J = 4-3/\text{H}^{13}\text{CN } J = 1-0$ intensity ratio, finding that the HVCCs have a higher density by an order of magnitude and possibly higher temperature than normal clouds in the CMZ.
4. Masses of CO–0.30–0.07 and CO–0.40–0.22 are estimated to be $2 \times 10^3 M_{\odot}$ and $4 \times 10^3 M_{\odot}$, respectively, from the $\text{H}^{13}\text{CN } J = 1-0$ and HCN $J = 4-3$ fluxes. Their kinetic energies are estimated to be $(0.8-2) \times 10^{49} \text{ erg}$ and $(1-4) \times 10^{49} \text{ erg}$. Kinetic energies of the molecular shells 1 and 2 are $1 \times 10^{51} \text{ erg}$ and $0.7 \times 10^{51} \text{ erg}$, respectively.
5. We examined several scenarios of the origin of the HVCCs, including cloud–cloud collisions caused by the expansion of the molecular shells, bipolar outflow from young massive stars, compact expanding shells driven by interaction with young SNRs, and ring/disks rotating around dark massive objects. The spatial resolution of our data is not sufficiently high to discriminate these scenarios, though absence of visible energy sources associated with the HVCCs may favor the cloud–cloud collision scenario.
6. More than 10 SN or two HN explosions in the last $2 \times 10^5 \text{ yr}$ are required to explain the kinetic energy of the expansion motion of each shell. This SN rate is interpreted into SFR of $(0.5-3) \times 10^{-2} M_{\odot} \text{ yr}^{-1}$ at 10^7 yr ago, which is about an order higher than the present SFR, but is close to the value in 10^{5-6} yr ago.

The authors are grateful to the NRO staffs for their generous support for our observations with the NRO 45 m and the ASTE 10 m telescopes. We also thank the anonymous referee, whose comments and suggestions were helpful in improving the paper.

REFERENCES

- Arikawa, Y., Tatematsu, K., Sekimoto, Y., Aso, Y., Noguchi, T., Shi, S. C., Miyazawa, K., Yamamoto, S., Ikeda, M., Maezawa, H., Ito, T., Saito, G., Saito, S., Ozeki, H., Fujiwara, H., Inatani, J., & Ohishi, M. 1999, in *Star Formation 1999*, ed. T. Nakamoto (Nagoya, Japan: Nobeyama Radio Observatory), 88
- Bachiller, R. & Cernicharo, J. 1990, *A&A*, 239, 276
- Bloemen, J. B. G. M., Strong, A. W., Blitz, L., Cohen, R. S., Dame, T. M., Grabelsky, D. A., Hermsen, W., Lebrun, F., Mayer-Hasselwander, H. A., & Thaddeus, P. 1986, *A&A*, 154, 25
- Caswell, J. L., Fuller, G. a., Green, J. a., Avison, a., Breen, S. L., Brooks, K. J., Burton, M. G., Chrysostomou, a., Cox, J., Diamond, P. J., Ellingsen, S. P., Gray, M. D., Hoare, M. G., Masheder, M. R. W., McClure-Griffiths, N. M., Pestalozzi, M. R., Phillips, C. J., Quinn, L., Thompson, M. a., Voronkov, M. a., Walsh, a. J., Ward-Thompson, D., Wong-McSweeney, D., Yates, J. a., & Cohen, R. J. 2010, *MNRAS*, 404, 1029
- Colbert, E. J. M. & Mushotzky, R. F. 1999, *ApJ*, 519, 89
- Dickman, R. L., Snell, R. L., Ziurys, L. M., & Huang, Y.-L. 1992, *ApJ*, 400, 203
- Diehl, R., Halloin, H., Kretschmer, K., Lichti, G. G., Schönfelder, V., Strong, A. W., von Kienlin, A., Wang, W., Jean, P., Knödlseider, J., Roques, J.-P., Weidenspointner, G., Schanne, S., Hartmann, D. H., Winkler, C., & Wunderer, C. 2006, *Nature*, 439, 45
- Ebisuzaki, T., Makino, J., Tsuru, G. T., Funato, Y., Portegies Zwart, S., Hut, P., Mcmillan, S. L. W., Matsushita, S., Matsumoto, H., & Kawabe, R. 2001, *ApJ*, 562, 19
- Fukui, Y., Yamamoto, H., Fujishita, M., Kudo, N., Torii, K., Nozawa, S., Takahashi, K., Matsumoto, R., Machida, M., Kawamura, A., Yonekura, Y., Mizuno, N., Onishi, T., & Mizuno, A. 2006, *Science*, 314, 106
- Gillessen, S., Eisenhauer, F., Trippe, S., Alexander, T., Genzel, R., Martins, F., & Ott, T. 2009, *ApJ*, 692, 1075
- Goldreich, P. & Kwan, J. 1974, *ApJ*, 190, 27
- Hüttemeister, S., Dahmen, G., Mauersberger, R., Henkel, C., Wilson, T. L., & Martín-Pintado, J. 1998, *A&A*, 334, 646
- Immer, K., Schuller, F., Omont, a., & Menten, K. M. 2012, *A&A*, 537, A121
- Jones, P. A., Burton, M. G., Cunningham, M. R., Requena-Torres, M. A., Menten, K. M., Schilke, P., Belloche, A., Leurini, S., Martín-Pintado, J., Ott, J., & Walsh, a. J. 2012, *MNRAS*, 419, 2961

- Jones, P. A., Burton, M. G., Cunningham, M. R., Tothill, N. F. H., & Walsh, a. J. 2013, MNRAS, 433, 221
- Jones, P. A., Burton, M. G., Tothill, N. F. H., & Cunningham, M. R. 2011, MNRAS, 411, 2293
- Kroupa, P. 2001, MNRAS, 322, 231
- Lang, C. C., Goss, W. M., Cyganowski, C., & Clubb, K. I. 2010, ApJS, 191, 275
- Langer, W. D. & Penzias, A., A. 1990, ApJ, 357, 477
- . 1993, ApJ, 408, 539
- LaRosa, T. N., Brogan, C. L., Shore, S. N., Lazio, T. J., Kassim, N. E., & Nord, M. E. 2005, ApJ, 626, L23
- Leurini, S., Schilke, P., Parise, B., Wyrowski, F., Güsten, R., & Philipp, S. 2006, A&A, 454, L83
- Lis, D. C. & Goldsmith, P. F. 1989, ApJ, 337, 704
- . 1990, ApJ, 356, 195
- Liszt, H. S. & Spiker, R. W. 1995, ApJS, 98, 259
- Martin, C. L., Walsh, W. M., Xiao, K., Lane, A. P., Walker, C. K., & Stark, A. A. 2004, ApJS, 150, 239
- Martín-Pintado, J., de Vicente, P., Fuente, A., & Planesas, P. 1997, ApJ, 482, L45
- Miyazaki, A. & Tsuboi, M. 2000, ApJ, 536, 357
- Moriguchi, Y., Yamaguchi, N., Onishi, T., Mizuno, A., & Fukui, Y. 2001, PASJ, 53, 1025
- Nagai, M., Tanaka, K., Kamegai, K., & Oka, T. 2007, PASJ, 59, 25
- Oka, T., Hasegawa, T., Sato, F., & Tsuboi, M. 2001, PASJ, 53, 787
- Oka, T., Hasegawa, T., Sato, F., Tsuboi, M., & Miyazaki, A. 1998, ApJS, 118, 445
- Oka, T., Hasegawa, T., White, G. J., Sato, F., Tsuboi, M., & Miyazaki, A. 2008, PASJ, 60, 429
- Oka, T., Nagai, M., Kamegai, K., Tanaka, K., & Kuboi, N. 2007, PASJ, 59, 15
- Oka, T., Onodera, Y., Nagai, M., Tanaka, K., Matsumura, S., & Kamegai, K. 2012, ApJS, 201, 14
- Oka, T., White, G. J., Hasegawa, T., Sato, F., Tsuboi, M., & Miyazaki, A. 1999, ApJ, 515, 249
- Pierce-Price, D., Richer, J. S., Greaves, J. S., Holland, W. S., Jennes, T., Lasenby, A. N., White, G. J., Matthews, H. E., Ward-Thompson, D., Dent, W. R. F., Zylka, R., Mezger, P., Hasegawa, T., Oka, T., Omont, A., & Gilmore, G. 2000, ApJ, 545, L121

- Portegies Zwart, S., Baumgardt, H., Hut, P., Makino, J., & Mcmillan, S. L. W. 2004, *Nature*, 428, 724
- Qiu, K., Wyrowski, F., Menten, K. M., Güsten, R., Leurini, S., & Leinz, C. 2011, *ApJ*, 743, L25
- Requena-Torres, M. A., Martín-Pintado, J., Rordíguez-Franco, N. J., Martín, S., Rordíguez-Fernández, N. J., & de Vicente, P. 2006, *A&A*, 455, 971
- Riquelme, D., Amo-Baladrón, M. a., Martín-Pintado, J., Mauersberger, R., Martín, S., & Bronfman, L. 2010a, *A&A*, 523, 51
- . 2013, *A&A*, 549, 36
- Riquelme, D., Bronfman, L., Mauersberger, R., May, J., & Wilson, T. L. 2010b, *A&A*, 523, 45
- Russeil, D. 2003, *A&A*, 146, 133
- Sashida, T., Oka, T., Tanaka, K., Aono, K., Matsumura, S., Nagai, M., & Seta, M. 2013, *ApJ*, 774, 10
- Schöier, F. L., Tak, F. F. S. V. D., Dishoeck, E. F. V., & Black, J. H. 2005, *A&A*, 379, 369
- Shetty, R., Beaumont, C. N., Burton, M. G., Kelly, B. C., & Klessen, R. S. 2012, *MNRAS*, 425, 720
- Tanaka, K., Kamegai, K., Nagai, M., & Oka, T. 2007, *PASJ*, 59, 323
- Tanaka, K., Oka, T., Matsumura, S., Nagai, M., & Kamegai, K. 2011, *ApJ*, 743, L39
- Tanaka, K., Oka, T., Nagai, M., & Kamegai, K. 2009, *PASJ*, 61, 461
- Torii, K., Kudo, N., Fujishita, M., Kawase, T., Yamamoto, H., Kwamura, A., Mizuno, N., Onishi, T., Mizuno, A., Machida, M., Takahashi, K., Nozawa, S., Matsumoto, R., & Fukui, Y. 2010, *PASJ*, 62, 1307
- Tsuboi, M., Handa, T., & Ukita, N. 1999, *ApJS*, 120, 1
- White, G. J. 1994, *A&A*, 283, L25
- Yusef-Zadeh, F., Goss, W. M., Roberts, D. A., Robinson, B., & Frail, D. A. 1999, *ApJ*, 527, 172
- Yusef-Zadeh, F., Hewitt, J. W., Arendt, R. G., Whitney, B., Rieke, G., Wardle, M., Hinz, J. L., Stolovy, S., Lang, C. C., Burton, M. G., & Ramirez, S. 2009, *ApJ*, 702, 178
- Yusef-Zadeh, F., Hewitt, J. W., & Cotton, W. 2004, *ApJS*, 155, 421